Nature Communications

https://doi.org/10.1038/s41467-026-70930-1

Article in Press

Copper single-atom nanozyme with intelligent capture and photo-enhanced activity for controlling plant bacterial diseases

Received: 16 December 2024

Accepted: 6 March 2026

Cite this article as: Jiang, H., Xing, Y., Ma, Z. *et al.* Copper single-atom nanozyme with intelligent capture and photo-enhanced activity for controlling plant bacterial diseases. *Nat Commun* (2026). https://doi.org/10.1038/s41467-026-70930-1

Hao Jiang, Yue Xing, Zhifeng Ma, Guangjin Fan, Zhongwei Liu, Song Yang & Lin Cai

Copper single-atom nanozyme with intelligent capture and photo-enhanced activity for controlling plant bacterial diseases

Hao Jiang[1,2,3], Yue Xing[1], Zhifeng Ma[2], Guangjin Fan[2], Zhongwei Liu[3], Song Yang[1], Lin Cai[2,*]

[1] National Key Laboratory of Green Pesticide, Key Laboratory of Green Pesticide and Agricultural Bioengineering, Ministry of Education, Center for R&D of Fine Chemicals of Guizhou University, Guiyang 550025, China.

[2] Guizhou Key Laboratory for Tobacco Quality, College of Tobacco Science of Guizhou University, Guiyang 550025, China.

[3] Institute of Agro-bioengineering, Guizhou University/Key Laboratory of Plant Resource Conservation and Germplasm Innovation in Mountainous Region (Ministry of Education), Guiyang 550025, China.

[*]Corresponding Author: lincai@gzu.edu.cn

Abstract

Nanozymes hold promise for controlling plant bacterial diseases, but conventional ones suffer from low bacterial affinity, inefficient enzyme-like activity, and thus poor antibacterial efficacy. Here, we report a photo-enhanced copper single-atom (CuSA)-loaded ZnS@MoS_2 nanozyme with high affinity and efficient peroxidase (POD)-like activity. CuSA-loaded ZnS@MoS_2 exhibits higher efficacies against bacterial speck and bacterial wilt diseases in tomatoes, surpassing the commercial thiodiazole copper by 13.33% and 52.77%, respectively. Mechanistically, it catalyzes H_2O_2 to generate toxic hydroxyl radicals (·OH) via POD-like activity; near-infrared irradiation boosts this activity by lowering activation energy and accelerating mass transfer. Density functional theory (DFT) calculations reveal that CuSA-loaded ZnS@MoS_2 captures bacteria via Metal-O-P bonds on cell surfaces, reducing ·OH short-range quenching to enhance efficacy. This SA nanozyme design, integrating intelligent capture and photo-enhanced activity, offers an insight for plant bacterial disease control.

Introduction

Plant bacterial diseases cause substantial annual crop yield losses, posing a severe threat to global food security[1, 2, 3]. For instance, *Pseudomonas syringae* pv. tomato DC3000 (*Pst*. DC3000) and *Ralstonia solanacearum* (*R. solanacearum*) are major pathogens limiting production of Solanaceae crops. The bacterial speck disease caused by *Pst*. DC3000 reduces the quality of tomatoes, resulting in a 75% reduction in their output, significantly impacting the global economy[4]. Similarly, *R. solanacearum* causes bacterial wilt disease, leading to yield reductions of 0-91% in tomato, 33-90% in potato, 10-30% in tobacco, and 80-100% in banana[5]. While agrochemicals are pivotal for controlling plant bacterial diseases[6], their escalating overuse and inherent inefficiency have driven a steady rise in bacterial resistance[7]. This resistance has further complicated disease control, creating an urgent need for efficient alternative antibacterial strategies.

Nanozymes, nanomaterials with enzyme-like activity, offer advantages including low cost, high stability, scalable production, and multifunctionality[8, 9, 10]. Peroxidase (POD)-like nanozymes are particularly promising: they catalyze the decomposition of H_2O_2 into hydroxyl radicals (·OH), the most effective reactive oxygen species (ROS) for eradicating pathogenic bacteria[11, 12, 13, 14]. This catalytic activity is well-matched to the microenvironment of plant infection sites, where pathogens induce the production of ROS (including H_2O_2) and organic acids[15, 16]. Notably, ~52% of sunlight consists of near-infrared (NIR) light; this enables NIR-enhanced nanozymes to kill bacteria more effectively by boosting their POD-like activity[17, 18]. POD-like nanozyme with NIR enhancement therefore represent a promising approach for controlling plant bacterial diseases. Structural modifications can further optimize antibacterial efficacy, such as loading exogenous metal atoms into a support matrix[19]. Single-atom (SA) nanozymes with precisely defined electronic and geometric structures are especially effective at mimicking the catalytic centers of natural enzymes[20, 21]. For example, CeO_2-supported Cu SA nanozymes demonstrated enhanced POD-like activity and reduced ·OH antioxidant capacity activity, effectively

combating Methicillin-resistant *Staphylococcus aureus* and *Escherichia coli*[19]. Nevertheless, the rapid quenching effect of ROS and the low affinity of SA nanozymes to the bacterial surface severely limit their applications[22]. Two-dimensional (2D) materials address these issues via multivalent binding: WS_2, MoS_2, and VO_xC nanosheets form strong Metal-O-P bonds with bacteria and possess membrane-conforming flexibility, thereby increasing the contact area and binding strength[22, 23, 24]. Complementary strategies involve ROS-generating metal ions (e.g., Zn^{2+}) that increase membrane permeability[25]. Integrating these advantages, a multifunctional Cu SA nanozyme combining NIR enhancement, optimized bacterial affinity via 2D support, and ROS-mediated membrane disruption could enable intelligent pathogen capture and kill in plant protection systems.

In this study, we develop a photo-enhanced CuSA-loaded ZnS@MoS_2 nanozyme with intelligent capture and killing bifunction through an atom loaded strategy. We evaluated this nanozyme for the control of tomato speck disease (caused by *Pst*. DC3000) and tomato bacterial wilt (caused by *R. solanacearum*), and investigated its antibacterial mechanism. Combined experimental and density functional theory (DFT) calculations demonstrate that CuSA-loaded ZnS@MoS_2 nanozyme exhibits high POD-like activity, efficiently catalyzing H_2O_2 to generate ·OH. This process is further enhanced under NIR irradiation. Additionally, CuSA-loaded ZnS@MoS_2 nanozyme can capture bacteria cells by interactions with the bacteria surface, avoiding the rapid quenching effect of ·OH. Benefiting from these advantages, CuSA-loaded ZnS@MoS_2 nanozyme achieves high efficacy in controlling plant bacterial diseases. These findings deepen the understanding of the antibacterial mechanism of SA nanozymes, guide the design of specific and efficient bactericidal nanozymes for plant disease control, and mark the pioneering application of SA nanozymes in the management of agricultural bacterial diseases.

Results and Discussion

Synthesis and characterization

Firstly, different amounts of Cu were added to synthesize the CuSA-loaded ZnS@MoS_2 using a conventional hydrothermal method (Fig. 1a). To identify the optimal Cu addition, we evaluated the POD-like catalytic activity of CuSA-loaded ZnS@MoS_2 and its effects on tomato seed germination. At a Cu addition of 0.25 mmol, CuSA-loaded ZnS@MoS_2 exhibited the highest POD-like activity and no toxicity to tomato seeds (Supplementary Fig. 1). Therefore, the addition of Cu used in all subsequent experiments was 0.25 mmol. As shown in Fig. 1b, CuSA-loaded ZnS@MoS_2 had an irregular overall morphology, with granular nanoparticles (NPs) distributed on the surface of lamellar structures. Supplementary Fig. 2 confirmed that these granular and lamellar components corresponded to ZnS and MoS_2, respectively. The zeta potential and average particle diameter of CuSA-loaded ZnS@MoS_2 were -23.86 mV and 513.09 nm, respectively (Supplementary Fig. 3). X-ray diffraction (XRD) patterns of CuSA-loaded ZnS@MoS_2 revealed characteristic peaks for ZnS (PDF#89-2156), MoS_2 (PDF#06-0097), and S (PDF#13-0141) (Supplementary Fig. 4). The high-resolution transmission electron microscopy (HRTEM), selected area electron diffraction (SAED) pattern, and Fast Fourier transformation (FFT) pattern indexing further confirmed the presence of three substances: ZnS (crystal plane: 102, interplanar spacing: 0.31 nm), S (crystal plane: 222, interplanar spacing: 0.33 nm), and MoS_2 (crystal plane: 002, interplanar spacing: 0.61 nm) (Supplementary Fig. 5). These lattice parameters matched the standard XRD data for ZnS, MoS_2, and S, confirming their crystalline phases. According to the previous report[26], we speculated that thioacetamide first reduced Cu^{2+} to Cu^{+}, then sulfurized MoO_3 to MoS_3. The subsequent reaction between MoS_3 and Cu^{+} produced MoS_2, Cu^{2+}, and S, which was confirmed by XRD pattern results. Meanwhile, the absence of nanocrystal and large clusters characteristic diffraction peaks for Cu suggested that Cu could exist in a single atomic form. To verify this, the high-angle annular dark field scanning transmission electron microscopy (HAADF-STEM) was employed to compare the atomic images of CuSA-loaded ZnS@MoS_2 and ZnS@MoS_2. However, it was difficult to clearly observe the presence of single Cu atoms in the HAADF-STEM images of CuSA-loaded ZnS@MoS_2. (Fig. 1c and Supplementary Fig. 6).

HAADF-STEM elemental mapping showed uniform distribution of Cu, Zn, O, Mo, and S across CuSA-loaded ZnS@MoS_2 (Fig. 1d). Due to HAADF-STEM's Z-contrast imaging was inherently limited when imaging high-Z (heavy) metals alongside low-Z (light) elements, the weak scattering intensity of low-Z elements made them undetectable in the presence of high-Z counterparts[27, 28, 29]. This likely explained the attenuated O signal in the elemental mapping. Fourier transform infrared (FTIR) spectrum results showed that the peaks at 452 cm^{-1}, 613 cm^{-1}, 899 cm^{-1}, 1049 cm^{-1}, 1126 cm^{-1}, 1388 cm^{-1}, 1612 cm^{-1}, and 3425 cm^{-1} were corresponding to the Metal-O[30], Metal-S[31], C-H[32], C-O[33], C-N[34], N-C-H[35], C=O[36], N-H/O-H, respectively (Supplementary Fig. 7). X-ray photoelectron spectroscopy (XPS) confirmed the elemental composition of CuSA-loaded ZnS@MoS_2, consistent with HAADF-STEM mapping (Supplementary Fig. 8a). Considering the critical role of element valence states, high-resolution XPS analysis of Mo 3*d*, Cu 2*p*, S 2*p*, Zn 2*p*, and O 1*s* was performed. The Mo 3*d* spectrum showed that two characteristic peaks at 229.3 eV and 228.6 eV were corresponding to the Mo^{4+} (Supplementary Fig. 8b)[37]. The characteristic peaks at 232 eV and 233.2 eV were corresponding to the Mo^{6+}[38]. The characteristic peak at 226.1 eV was attributed to the presence of sulfur 2*s*[39]. Furthermore, the characteristic peaks observed in the Cu 2*p* at 932.4 eV and 952.3 eV were ascribed to Cu^{+}[40, 41], while the peak detected at 946.3 eV were assigned to weak satellite peak (Supplementary Fig. 8c)[42]. As shown in Supplementary Fig. 8d, three characteristic peaks at 162.6 eV, 168.9 eV, and 161.4 eV were assigned to Mo-S, S in thiosulfate and sulfate, and Cu/Zn-S, respectively[43]. This suggested that the material could present a Cu-S-Zn structure. The Zn 2*p* was divided into the characteristic peaks at 1021.7 eV, 1044.7 eV, and 1038.2 eV, attributing to Zn $2p_{3/2}$ and Zn $2p_{1/2}$, respectively (Supplementary Fig. 8e)[44, 45, 46]. The O 1*s* spectrum exhibited three characteristic peaks at 531.7 eV, 530.5 eV, and 533.0 eV corresponding to the binding energy of Metal-O, lattice-O, and surface-adsorbed water, respectively (Supplementary Fig. 8f)[47, 48]. Inductively coupled plasma optical emission spectrometry (ICP-OES) quantified the elemental contents: Cu (11.4 wt%), Zn (27.5 wt%), and Mo (11.9 wt%) (Supplementary Fig. 9). Collectively, these results confirmed the successful synthesis of

CuSA-loaded ZnS@MoS_2 with a Cu-S-Zn structure.

Coordination chemistry states of Cu single atom

To resolve the coordination chemistry states of CuSA, the X-ray absorption near-edge structure (XANES) and extended X-ray absorption fine structure (EXAFS) measurements were performed[14]. The XANES spectra at the K-edge revealed that the pre-edge of Cu in CuSA-loaded ZnS@MoS_2 was situated between that of CuO and Cu_2O as well as between that of CuS and Cu_2S, demonstrating the oxidation state of Cu atoms in CuSA-loaded ZnS@MoS_2 was higher than Cu^+ and lower than Cu^{2+} (Fig. 1e and Supplementary Fig. 10). The Fourier-transformed (FT) $\mathbf{k}^3$-weighted extended XAFS (FT-EXAFS) spectrum of CuSA-loaded ZnS@MoS_2 displayed the dominant peak at ~1.5 Å, which could be mainly attributed to the scattering interactions between Cu and N/O atoms (Fig. 1f)[49]. Furthermore, the R space showed the peak at ~2.0 Å corresponding to the scattering interactions between Cu and S atoms (Fig. 1f). Notably, no prominent Cu-Cu coordination peak (typically at ~2.2 Å, as observed in Cu foil) was detected. This confirmed Cu existed as isolated single atoms in CuSA-loaded ZnS@MoS_2, with no aggregation into clusters or NPs. To quantify the Cu coordination environment, we performed least-squares EXAFS curve fitting. The fitting curves and parameters were provided in Fig. 1g and Supplementary Fig. 11, and Supplementary Table 1. The fitting results indicated that the coordination number of Cu-N/O (average bond length: 1.959 Å) and Cu-S (average bond length: 2.409 Å) were 5.9 ± 0.3 and 0.5 ± 0.1, respectively. Wavelet transform (WT) analysis of the Cu K-edge EXAFS provided further validation of this conclusion, explicitly confirming both the isolated Cu-S coordination and the lack of Cu-Cu aggregation (Fig. 1h-j).

Photothermal and enzyme-like properties

To evaluate the photothermal performance of CuSA-loaded ZnS@MoS_2, we recorded temperature changes during NIR irradiation. Under 808 nm NIR light, the temperature of CuSA-loaded ZnS@MoS_2 suspensions increased in a concentration-dependent manner (Fig. 2a). The photothermal conversion

efficiency (η) was calculated using a 200 μg/mL CuSA-loaded ZnS@MoS_2 suspension (1 mL): the sample was irradiated with an 808 nm laser (1 W/cm^2) for 10 min until temperature plateaued, then cooled to initial temperature under ambient conditions. The η value of CuSA-loaded ZnS@MoS_2 was 15.37% (Fig. 2b, see the Supplementary Information for details). Although this η was lower than that of commonly used photothermal materials[50], CuSA-loaded ZnS@MoS_2 still raised the system temperature from 25°C to 40°C under the above irradiation conditions. This temperature was close to the optimal working temperature of natural enzymes[51, 52], meaning it avoided damaging plant cells while promoting catalytic reactions via increased thermal energy.

Previous reports indicated that nanozymes with OXD-like activity or POD-like activity could oxidize 3,3,5,5-tetramethylbenzidine (TMB) to blue oxTMB[14, 53]. Thus, we evaluated the potential OXD-like activity of the material. It is well known that O_2 could be catalyzed by the OXD-like activity of Cu^+ to generate $O_2^{\cdot-}$, which oxidized TMB to oxTMB[54]. However, CuSA-loaded ZnS@MoS_2 and MoS_2 displayed no obvious OXD-like activity (Supplementary Fig. 12). This might be attributed to the relatively low concentration of dissolved oxygen molecules in the liquid phase system[55]. Subsequently, the POD-like activity of CuSA-loaded ZnS@MoS_2 was determined using a typical biochemical reaction of TMB[56]. The POD-like activity of these materials was evaluated under different pH values. As shown in Supplementary Figs. 13 and 14, CuSA-loaded ZnS@MoS_2 presented a more intensive activity than the MoS_2 nanosheets, and ZnO NPs displayed no obvious POD-like activity. The POD-like activity of CuSA-loaded ZnS@MoS_2 and MoS_2 gradually decreased with increased pH value. In addition, NIR irradiation could enhance the POD-like activity of CuSA-loaded ZnS@MoS_2 (Fig. 2c). According to the Arrhenius equation, higher temperatures increase reaction rates by lowering activation energy and accelerating mass transfer[17]. This explained the NIR-induced activity enhancement, as photothermal heating raised the system temperature. Furthermore, the maximum initial velocity (V_{max}), Michaelis constant (K_m), and turnover number (TON, the maximum number of transforming substrate molecules per catalytic site) were

calculated based on the Michaelis-Menten curves (Fig. 2d, e and Supplementary Figs. 15 and 16). The V_{max} and K_m values of CuSA-loaded ZnS@MoS_2 for TMB were 2.78×10^{-8} M/s and 0.43×10^{-3} M, respectively (Supplementary Fig. 15). The V_{max}, K_m, and TON values of CuSA-loaded ZnS@MoS_2 for H_2O_2 were 1.62×10^{-7} M/s, 2.37×10^{-2} M, and 2.30×10^{-3} s^{-1}, respectively (Supplementary Fig. 16 and Supplementary Table 2). A previous study reported a CuSA-loaded MoS_2 nanozyme with POD-like activity, synthesized via machine learning-guided electrostatic self-assembly[57]. However, this method relied on weak electrostatic interactions between Cu^{2+} and MoS_2, limiting Cu^{2+} binding strength and catalytic capacity. By contrast, the V_{max} value of our synthesized CuSA-loaded ZnS@MoS_2 was over 1000 times higher than the reported value, which could be attributed to the predominantly monovalent valence state of the CuSA. We further compared CuSA-loaded ZnS@MoS_2 to reported artificial PODs (metal oxides, metal hydrides, single-atom catalysts, metal complexes) (Fig. 2f, Supplementary Table 2). Our nanozyme exhibited the highest V_{max} and TON, confirming its stronger ability to mimic natural POD. Electron paramagnetic resonance (EPR) spectroscopy confirmed that CuSA-loaded ZnS@MoS_2 and MoS_2 in the presence of H_2O_2 appeared the characteristic signal of DMPO·OH with an intensity ratio of 1:2:2:1 (Fig. 2g). The signal intensity was significantly stronger for CuSA-loaded ZnS@MoS_2, confirming it produces more ·OH. The detailed mechanisms were shown in Fig. 2h.

To elucidate the POD-like catalytic mechanism and selective ·OH production activity of CuSA-loaded ZnS@MoS_2, we performed the DFT to calculate the catalysis system. Based on the aforementioned characterization results, we established two models of CuSA-loaded ZnS@MoS_2, featuring Cu-N/O coordination and Cu-S coordination, respectively (Fig. 3a, 3b, and Supplementary Fig. 17). As shown in Fig. 3c, 3d, and 3e, the initial adsorption of H_2O_2 and its subsequent decomposition into 2*OH on the ZnS surface of Cu-N/O coordination model and the Cu site of Cu-S coordination model exhibited negative changes in Gibbs free energy, indicating that these two steps were spontaneous processes on both types of catalyst surfaces. Furthermore, the Gibbs free energies for the desorption of 2*OH were calculated to

be 3.96 eV for Cu site of Cu-S coordination model and 4.48 eV for ZnS surface of Cu-N/O coordination model. This indicated a weaker binding affinity of OH on the Cu site of Cu-S coordination model, which facilitated the release of ·OH. Finally, we also elucidated the behavior of electrons in the pivotal process, delving into their intricate and nuanced actions (Fig. 3f). The oxygen atom of H_2O_2 initially captured an electron from Cu(I) in the 3*d* orbital. Subsequently, a homogeneous splitting of the σ bond in H_2O_2 occurred, leading to the generation of hydroxide and ·OH. With releasing the ·OH, the electron pair of the hydroxide effectively attacked the vacant 4*s* orbital of Cu(II), leading to the formation of a new σ bond. This process occurred with greater ease compared to Mo(IV) donating an electron.

In summary, CuSA-loaded ZnS@MoS_2 nanozyme efficiently converted low-toxic H_2O_2 into highly toxic ·OH. Under NIR irradiation, its POD-like activity was further enhanced by photothermal heating, which lowered the reaction activation energy. This dual capability (catalytic ·OH generation and NIR-enhanced activity) enabled localized production of potent ROS, thereby boosting bactericidal efficacy.

In vitro antibacterial activity and mechanism

Encouraged by the catalytic activity and ROS generation mechanism of CuSA-loaded ZnS@MoS_2 nanozyme, we performed *in vitro* antibacterial assays. The representative strains *Pst*. DC3000 and *R. solanacearum*, two devastating Gram-negative bacteria infecting the leaves and roots of Solanaceae, were chosen as the study subjects. For comparison, we used the commercial bactericide thiodiazole copper (a widely used agricultural antibacterial agent). As shown in Fig. 4a, c and Supplementary Figs. 18, 19, 20, CuSA-loaded ZnS@MoS_2 inhibited *Pst*. DC3000 and *R. solanacearum* in a dose-dependent manner, outperforming thiodiazole copper at all tested concentrations. Consistent with this, the half-maximal effective concentration (EC_{50}) of CuSA-loaded ZnS@MoS_2 against both pathogens were lower than that of thiodiazole copper, confirming its higher antibacterial activity (Supplementary Table 3). CuSA-loaded ZnS@MoS_2 also showed better inhibition than CuO NPs, ZnO NPs, and MoS_2 nanosheets (Supplementary Figs. 21, 22). Furthermore, it outperformed CuSA@MoS_2 and ZnS@MoS_2

(Supplementary Figs. 23, 24, 25, and 26), indicating a synergistic antibacterial effect between CuSA and ZnS in the nanozyme. To optimize the POD-like catalytic condition for antibacterial assays, we first determined the optimal H_2O_2 concentrations for *Pst*. DC3000 (100 μM) and *R. solanacearum* (10 μM) by testing H_2O_2's intrinsic antibacterial effect (Supplementary Figs. 27, 28). Under these optimal H_2O_2 conditions, CuSA-loaded ZnS@MoS_2 increased the inhibition rate of *Pst*. DC3000 and *R. solanacearum* by 69.71% and 87.63%, respectively, compared to the H_2O_2-only control (Fig. 4b and Supplementary Figs. 29, 30). To verify that ·OH was the primary contributor to antibacterial activity, we performed ·OH scavenging assays using tert-butanol (TBA). Under H_2O_2 conditions, the addition of TBA significantly reduced the antibacterial activity of CuSA-loaded ZnS@MoS_2 nanozyme, suggesting that the ·OH generation during catalysis was the primary contributor of antibacterial activity (Supplementary Figs. 31, 32). Then, the ·OH generation capabilities of CuSA-loaded ZnS@MoS_2 nanozyme at 2.5 μg/mL and 12.5 μg/mL were measured to be 9.44 U/mL and 16.16 U/mL, respectively (Supplementary Fig. 33a). To rule out Cu ion leaching as a contributing factor, we measured Cu ion release from CuSA-loaded ZnS@MoS_2 after 2 h and tested the antibacterial activity of this leached Cu concentration. No significant inhibition was observed, confirming the antibacterial mechanism was not dependent on Cu ion release (Supplementary Fig. 34). Given the NIR-enhanced POD activity of CuSA-loaded ZnS@MoS_2 nanozyme, it had great potential in plant leaf bacterial disease control[18]. The NIR irradiation not only improved the antibacterial ability of CuSA-loaded ZnS@MoS_2 nanozyme against *Pst*. DC3000, but also further boosted activity under H_2O_2 conditions (Fig. 4b and Supplementary Fig. 29). These phenomena could be attributed to the fact that NIR irradiation reduced the activation energy required for POD-like catalytic reactions, making it easier to catalyze the conversion of H_2O_2 into highly toxic ·OH.

To confirm intracellular ROS generation, we stained *Pst*. DC3000 and *R. solanacearum* with ROS-specific dyes and analyzed fluorescence intensity. CuSA-loaded ZnS@MoS_2 nanozyme treatment significantly increased ROS fluorescence intensity, suggesting that the nanozyme induced intracellular

ROS generation in both bacteria (Fig. 4d, e and Supplementary Fig. 33b, c). NIR irradiation further enhanced fluorescence, confirming NIR amplifies ROS generation (Fig. 4d). SEM images revealed the morphological changes of *Pst*. DC3000 and *R. solanacearum* after different treatments. As shown in Fig. 4f, the cell surface contraction in *Pst*. DC3000 was gradually apparent after treatments with NIR, H_2O_2, and NIR + H_2O_2. Compared with the control, CuSA-loaded ZnS@MoS_2 nanozyme caused the stretching and squeezing of *Pst*. DC3000 cells. NIR and H_2O_2 treatments aggravated the CuSA-loaded ZnS@MoS_2 nanozyme on the disruption of *Pst*. DC3000 cells (Fig. 4f). For *R. solanacearum*, H_2O_2 did not cause noticeable damage on the surface of *R. solanacearum* cells, compared to the control (Fig. 4g). Additionally, CuSA-loaded ZnS@MoS_2 nanozyme caused the tearing of *R. solanacearum* cells. Under H_2O_2 conditions, the ·OH generated by the POD-like catalytic activity of CuSA-loaded ZnS@MoS_2 nanozyme severely disrupt the *R. solanacearum* cells. Then, the alteration of the bacterial contents after these treatments were determined. The results were generally consistent with the findings obtained from the bacterial plate assays (Supplementary Fig. 35). Notably, CuSA-loaded ZnS@MoS_2 nanozyme caused the morphological change of *Pst*. DC3000 cells and *R. solanacearum* cells. It is reported that cationic micellar nanostructures were also employed to disrupt the membrane of methicillin-resistant *Staphylococcus aureus* and fungi through steric hindrance, hydrogen bonding, and electrostatic interaction with the cell wall/membrane[58]. Previous studies also showed that 2D VO_xC nanosheets bound strongly to lipopolysaccharide (LPS, a major component of Gram-negative outer membranes) via phosphate group interactions[22]. Therefore, we hypothesized CuSA-loaded ZnS@MoS_2 nanozyme bound to bacterial surface components, causing bacterial stretching and squeezing or tearing.

Based on this hypothesis, we used DFT to calculation the binding affinity of two CuSA-loaded ZnS@MoS_2 nanozyme models (Cu-N/O and Cu-S coordination) for adsorbing inorganic cations (Na^+, K^+, Mg^{2+}, Ca^{2+}, and Zn^{2+}), anions (Cl^-, NO_3^-, PO_4^{3-}, SO_4^{2-}, and SO_3^{2-}), and organic functional groups (-COOH and -NH_2) commonly found on the bacterial surface. Both models showed stronger adsorption for PO_4^{3-}

than other ions (Fig. 4h, 4i). Specifically, Cu-S coordination model was stronger adsorption for PO_4^{3-}, Zn^{2+}, SO_3^{2-}, SO_4^{2-}, Mg^{2+}, Ca^{2+}, -NH_2, -COOH, and K^+. Cu-N/O coordination model was stronger adsorption for NO_3^-, Cl^-, and Na^+. These results reflected the nanozyme's complex surface charge, driven by both coordination structures. The strong PO_4^{3-} adsorption suggested that the binding to bacterial surfaces was primarily mediated by Metal-O-P bonds (interacting with LPS/phospholipid phosphates). To validate this, the nanozyme's binding to LPS and PO_4^{3-} were measured. CuSA-loaded ZnS@MoS_2 nanozyme exhibited a stronger affinity for LPS than PO_4^{3-}, confirming its high bacterial affinity (Supplementary Fig. 36), in agreement with previous reports.[22] We further tested PO_4^{3-} in plant apoplastic sap (a potential competitor); even so, the nanozyme retained stronger bacterial affinity (Supplementary Fig. 37). This "intelligent binding" shortened ·OH diffusion distance, enabling direct bacterial contact and efficient killing. Membrane permeability assays showed NIR did not increase permeability, suggesting permeability changes were driven by the nanozyme itself (Supplementary Figs. 38, 39). Given Zn^{2+} enhanced permeability via ROS[25], we proposed the nanozyme's permeability effect arose from both bacterial surface binding and ZnS-derived Zn^{2+}. Furthermore, we also explored the nanozyme's antibacterial mechanism by assessing bacterial motility, antioxidant enzyme (superoxide dismutase (SOD), catalase (CAT)) activity, biofilm formation, and extracellular polysaccharide (EPS) production. The results showed that CuSA-loaded ZnS@MoS_2 nanozyme reduced motility, decreased SOD and CAT activity, inhibited biofilm formation, and lowered EPS production in both bacteria (Supplementary Figs. 40, 41, 42).

In summary, as shown in Fig. 4j, the main antibacterial mechanisms of CuSA-loaded ZnS@MoS_2 nanozyme were as follows: (1) The nanozyme bound to the bacterial cell wall/outer membrane (via Metal-O-P bonds with LPS/phospholipids), anchoring to bacteria. (2) Binding stimulates intracellular ROS production and alters bacterial membrane permeability. (3) The nanozyme catalyzed H_2O_2 to produce highly toxic ·OH through POD-like activity. (4) NIR irradiation lowered POD catalytic activation energy

and accelerated mass transfer, further boosting ·OH production and antibacterial efficacy. (5) The nanozyme could reduce motility, decreased antioxidant enzyme activities, inhibited biofilm formation, and lowered EPS production in bacteria. These mechanisms collectively drived the nanozyme's high antibacterial efficiency.

Biosafety

Nanomaterials were promising for improving plant growth, crop yields, and disease resistance[59, 60, 61]; however, their inevitable release into agricultural environments during application raised biosafety concerns. Therefore, the biosafety of nanomaterials to plants should be evaluated before practical applications. We preliminarily evaluated the leaching behavior of Cu^{2+} in CuSA-loaded ZnS@MoS_2 nanozyme (200 μg/mL) at different pH levels (pH 5 and pH 7) and in different solutions (water and PBS) over different time intervals (1 d, 3 d, 5 d, and 8 d) (Supplementary Fig. 43). The results demonstrated that CuSA-loaded ZnS@MoS_2 nanozyme exhibited the highest concentration of Cu^{2+} release at pH 5, reaching a maximum of 8.62 μg/mL. At both pH 7 and in water, the release of Cu^{2+} remained relatively stable. In contrast, the amount of Cu^{2+} released in PBS was below the detection limit of ICP-OES, indicating that the release of Cu^{2+} in PBS was minimal. We next assessed the CuSA-loaded ZnS@MoS_2 nanozyme's safety to Solanaceae plants (tomato, tobacco) and human cells. Exposure to CuSA-loaded ZnS@MoS_2 had no significant effect on plant height, root length, shoot biomass, or seed germination rate (Supplementary Figs. 44, 45, and 46). CuSA-loaded ZnS@MoS_2 nanozyme also demonstrated no cytotoxic effects on human gut cell lines (Caco-2 cells) across a range of concentrations (0, 10, 20, 50, 100, and 200 μg/mL), indicating its biosafety (Supplementary Fig. 47). However, CuSA-loaded ZnS@MoS_2 nanozyme at 400 μg/mL exhibited low toxicity towards Caco-2 cells. These results indicated that CuSA-loaded ZnS@MoS_2 nanozyme had potential biosafety for Solanaceae plants and human cells. Furthermore, the acute toxicity of CuSA-loaded ZnS@MoS_2 nanozyme on non-target organisms, including zebrafish and earthworms, was evaluated. The results indicated that the nanozyme at 20 μg/mL

and 200 μg/mL exhibited no significant difference in survival rates of zebrafish and earthworms (Supplementary Fig. 48), confirming the safety of CuSA-loaded ZnS@MoS_2 nanozyme for non-target organisms. We also evaluated the effects of CuSA-loaded ZnS@MoS_2 nanozyme on root endosphere, rhizosphere soil microbes, and leaf endosphere microbes, as well as the effects of CuSA-loaded ZnS@MoS_2 nanozyme + NIR on leaf endosphere microbes. The results indicated that the antibacterial efficacy and photothermal effects of CuSA-loaded ZnS@MoS_2 nanozyme had a minimal impact on microbes in plants and in the environment, preliminarily confirming the safety of CuSA-loaded ZnS@MoS_2 nanozyme (Supplementary Figs. 49, 50, and 51). To further confirm that the application concentration of CuSA-loaded ZnS@MoS_2 nanozyme was non-toxic to tomato plants, we assessed the malondialdehyde (MDA) content, SOD activity, POD activity, and CAT activity in tomato plant leaves after foliar application at 200 μg/mL and roots after root application at 20 μg/mL. The results indicated that CuSA-loaded ZnS@MoS_2 nanozyme did not induce oxidative damage to the tomato plants (Supplementary Fig. 52). Similarly, we found that foliar application of 200 μg/mL nanozyme + 100 μM H_2O_2 and root application of 20 μg/mL nanozyme + 10 μM H_2O_2 did not induce oxidative damage in tomato plants. This indicated that the ·OH of catalytic production by nanozymes from H_2O_2 did not pose any harm to the plants (Supplementary Fig. 53). Notably, we observed that the foliar or root application of CuSA-loaded ZnS@MoS_2 nanozyme could induce plant immunity by upregulating the expression of *NPR1*, *PR1b1*, and *PR5* genes (Supplementary Figs. 54, 55). We also evaluated the changes in the contents of Cu, Zn, and Mo elements in both plants and soil after the foliar application and root application of CuSA-loaded ZnS@MoS_2 nanozyme. Foliar application of CuSA-loaded ZnS@MoS_2 nanozyme facilitated the uptake of Zn and Mo elements by the roots, as well as the uptake of Cu, Zn, and Mo elements by the shoots (Supplementary Fig. 56). However, there were no significant changes in the concentrations of Cu, Zn, and Mo elements in the soil. Root application of CuSA-loaded ZnS@MoS_2 nanozyme facilitated the uptake of Cu and Zn by the roots and Cu and Mo by the shoots, while also

increasing the soil content of Zn and Mo (Supplementary Fig. 57).

The degradation of nanomaterials in the environment was crucial for assessing their biosafety. Thus, we evaluated the degradation of CuSA-loaded ZnS@MoS_2 nanozyme in soil and the infectious environment around bacteria according to the previous reports[62, 63]. The results indicated that over time, Cu in the nanozyme primarily existed as residual fraction and organic-bound fraction; Zn predominantly occurred as Fe-Mn oxides-bound fraction and organic-bound fraction; while Mo was mainly found in the form of organic-bound fraction (Supplementary Fig. 58). Furthermore, malic acid, H_2O_2, and horseradish peroxidase (HRP) + H_2O_2 could promote the oxidation of CuSA-loaded ZnS@MoS_2 nanozyme (Supplementary Figs. 59, 60, 61). However, the presence of Cu^+, Mo^{4+}/Mo^{6+}, and S^{2-} within the CuSA-loaded ZnS@MoS_2 nanozyme increased complexity to the system, which was confirmed through XPS and previous reports regarding H_2O_2 and HRP + H_2O_2 interactions[63, 64]. Therefore, soil and infectious environment around bacteria could gradually degrade the CuSA-loaded ZnS@MoS_2 nanozyme, suggesting that the nanozyme possessed potential biosafety and long-term efficacy in controlling bacterial diseases.

In vivo antibacterial activity

Based on the conclusions above, CuSA-loaded ZnS@MoS_2 nanozyme was utilized via foliar spraying (to control tomato bacterial speck disease) and root irrigation (to control tomato bacterial wilt disease). To verify the catalytic activity of CuSA-loaded ZnS@MoS_2 nanozyme within plants, the H_2O_2 content at the infection sites was measured. The results indicated that the H_2O_2 contents at the infection sites of both tomato speck disease and wilt disease were higher than the concentrations used in our *in vitro* experiments (Supplementary Fig. 62). Therefore, CuSA-loaded ZnS@MoS_2 nanozyme could achieve catalyze activity within plant tissues. Uptake and distribution of CuSA-loaded ZnS@MoS_2 nanozyme in plants further confirmed the accumulation of nanozyme in apoplast, enabling the reduction of bacterial colonization within plant tissues (Supplementary Figs. 63, 64, 65). These results provided evidence that

CuSA-loaded ZnS@MoS_2 nanozyme could effectively control tomato speck disease and wilt disease. *In vivo* experiments results indicated that CuSA-loaded ZnS@MoS_2 nanozyme could significantly decrease the disease index of tomato speck disease, resulting in 21.67% disease index at 7 dpi (Fig. 5a, c), whereas the control was 83.33%, ZnO NPs was 51.67%, MoS_2 nanosheets was 41.67%, CuO NPs was 38.33%, and commercial bactericide thiodiazole copper was 35%. The leaf disc assay also demonstrated the excellent curative efficacy of CuSA-loaded ZnS@MoS_2 nanozyme against tomato speck disease (Supplementary Fig. 66). Furthermore, CuSA-loaded ZnS@MoS_2 nanozyme under NIR irradiation also exhibited better curative effect than CuSA-loaded ZnS@MoS_2 nanozyme-alone treatment (Supplementary Fig. 67). For tomato wilt disease, the disease index after CuSA-loaded ZnS@MoS_2 nanozyme treatment was obviously reduced, resulting in 31.67% disease index at 10 dpi (Fig. 5b, d), whereas the control was 100%, ZnO NPs was 60%, MoS_2 nanosheets was 91.67%, CuO NPs was 63.33%, and commercial bactericide thiodiazole copper was 75%. These results indicated that CuSA-loaded ZnS@MoS_2 nanozyme exhibited stronger curative activity against tomato speck disease and tomato wilt disease within a short period. To evaluate the long-term control effect of CuSA-loaded ZnS@MoS_2 nanozyme, the stability of the nanozyme was assessed under various conditions, including different temperatures (4°C and 25°C), different pH levels (pH 5, pH 7, and pH 9), different solvent types (water, ethanol, and PBS), as well as different time (1 d, 7 d, 14 d, 21 d, and 28 d). The results indicated that CuSA-loaded ZnS@MoS_2 nanozyme exhibited excellent stability under various conditions (Supplementary Fig. 68). Furthermore, the homogeneity of CuSA-loaded ZnS@MoS_2 nanozyme in water was also important to the practical applications[65]. The Tyndall effect and polydispersity index were utilized to investigate the homogeneity of nanozyme in solution. The results indicated that the nanozyme was uniformly dispersed in water over a short term (Supplementary Fig. 69). Finally, the disease index of CuSA-loaded ZnS@MoS_2 nanozyme against tomato speck disease and wilt disease significantly decreased by 41.67% and 36.67% at 20 dpi, respectively (Supplementary Fig. 70). Therefore, CuSA-

loaded ZnS@MoS_2 nanozyme demonstrated a sustained ability to effectively control tomato speck disease and wilt disease.

In summary, we develop a CuSA-loaded ZnS@MoS_2 nanozyme with highly efficient POD-like and NIR-enhanced activities for the control of tomato bacterial speck and tomato bacterial wilt diseases. CuSA-loaded ZnS@MoS_2 nanozyme shows higher activities than other reported POD-like nanozyme. Experimental studies and theoretical calculations demonstrate that CuSA-loaded ZnS@MoS_2 nanozyme can achieve the "capture and kill" bifunctionality by binding to the cell wall/outer membrane. Additionally, NIR irradiation can enhance the POD-like activity of CuSA-loaded ZnS@MoS_2 nanozyme by decreasing the activation barrier and increasing the mass transfer rate. *In vivo* bioassay results show that the phytotoxicity-free CuSA-loaded ZnS@MoS_2 nanozyme can effectively inhibit tomato speck disease and tomato wilt disease, and its curative effect is higher to that of the commercial bactericide thiodiazole copper. These findings uncover the photo-enhanced activity and smart capture mechanism of SA nanozymes, deepening the understanding of their antibacterial mechanisms, providing a strategy for designing highly efficient and specific antibacterial nanozymes.

Methods

Ethical regulations

This research complies with all relevant ethical regulations, and the study protocols are approved by the Subcommittee of Experimental Animal Ethics Committee of Guizhou University (Protocol No. EAE-2025-E063).

Synthesis of CuSA-loaded ZnS@MoS_2 nanozyme

The CuSA-loaded ZnS@MoS_2 nanozyme was synthesized via a hydrothermal method. Briefly, 0.6 mmol of ZnO NPs, 0.25 mmol $Na_2MoO_4 \cdot 2H_2O$, 0.03125-0.5 mmol $C_4H_8CuO_5$, and 3 mmol C_2H_5NS were mixed in 50 mL of ultrapure water through sonication treatment for a duration of 30 min. The mixture

was subsequently transferred into a 100 mL Teflon-lined stainless-steel autoclave and subjected to heating at 220°C for 12 h. After being cooled to room temperature, the obtained sample was thoroughly washed three times with water and ethanol, respectively. During the separation process, the centrifugal force was 10911 × g and the duration was 10 min. Finally, the product was dried in an oven at 70°C for 8 h.

POD-like activity of CuSA-loaded ZnS@MoS_2 nanozyme

The POD-like activity of CuSA-loaded ZnS@MoS_2 nanozyme was evaluated by employing TMB as the substrate in the presence of H_2O_2. The OD_{652} value was recorded to determine the POD-like activity. CuSA-loaded ZnS@MoS_2 nanozyme (500 μg/mL, final concentration), TMB (1 mM, final concentration), and H_2O_2 (200 mM, final concentration) were added to 0.1 M PBS (pH 5.5) and were incubated for 5 min. For steady-state kinetics assays, the system contained 500 μg/mL CuSA-loaded ZnS@MoS_2 nanozyme in the presence of TMB and H_2O_2. 1) TMB as the substrate: 200 mM H_2O_2 and different concentrations of TMB (50, 100, 200, 500, 700, and 800 μM) were added to the system containing CuSA-loaded ZnS@MoS_2 nanozyme and were incubated for 5 min. 2) H_2O_2 as the substrate: 1 mM TMB and different concentrations of H_2O_2 (1, 2, 5, 10, 15, 20, 25, 30, 35, and 40 mM) were added to the system containing CuSA-loaded ZnS@MoS_2 nanozyme and were incubated for 5 min. The reaction rates were plotted against their corresponding concentrations of H_2O_2 or TMB and then fitted with the Michaelis-Menten curves. Additionally, a Lineweaver-Burk plot was utilized to determine the values of V_{max} and K_m. Furthermore, the turnover number (TON) was calculated according to equation (1).

$$\mathrm{TON} = V_{max}/[E_0] \quad (1)$$

$[E_0]$ is the molar concentration of metal in nanozymes.

NIR enhanced the POD-like activity of CuSA-loaded ZnS@MoS_2 nanozyme

The different treatments were set as: TMB (1 mM, final concentration), TMB (1 mM, final concentration) + H_2O_2 (200 mM, final concentration), TMB (1 mM, final concentration) + CuSA-loaded ZnS@MoS_2 nanozyme (500 μg/mL, final concentration), and TMB (1 mM, final concentration) + H_2O_2

(200 mM, final concentration) + CuSA-loaded ZnS@MoS_2 nanozyme (500 μg/mL, final concentration) were added to 0.1 M PBS (pH 5.5) and were incubated for 5 min under NIR or no NIR irradiation, respectively. Then, the OD_{652} values were measured.

***In vitro* antibacterial activity assay**

Foliar plant pathogen (*Pst.* DC3000): According to the previous method, the antibacterial experiments were performed with some modifications[12]. Briefly, *Pst*. DC3000 cells were incubated in King's B (KB) medium (glycerol 1%, peptone 20 g/L, K_2HPO_4 1.5 g/L, $MgSO_4 \cdot 7H_2O$ 1.5 g/L, and rifampicin 25 mg/L) with shaking at 28°C and 180 rpm for 48 h. The obtained bacterial suspension (OD_{600} = 1.0) was diluted to 10^4 or 10^5. The bacterial suspension (200 μL) was then mixed with varying concentrations of nanomaterial suspensions (200 μL) in 2 mL centrifuge tubes. The mixed solution was incubated in the dark at 28°C for 2 h. The mixed solution was spread onto the KB solid medium plate using 50 μL. After incubating at a temperature of 28°C for a duration of 24 h, the colony-forming units (CFUs) were quantified and recorded. The inhibition rates of different concentrations CuSA-loaded ZnS@MoS_2 nanozyme and thiodiazole copper against *Pst*. DC3000 were utilized to calculate the EC_{50} values. The antibacterial activity of the nanomaterials was tested by a colony-counting method. The inhibition rate (%) was calculated as follows:

$$\text{Inhibition rate } (\%) = \frac{A_0 - A}{A_0} \times 100 \quad (2)$$

where A_0 represents the number of CFU on the control plates, and A represents the number of CFU after using different concentrations of the sample treatment.

The H_2O_2 concentration was optimized to investigate the antibacterial activity of CuSA-loaded ZnS@MoS_2 nanozyme based on its POD-like properties and NIR-induced photothermal effect. The above diluted bacterial suspension was incubated with different concentrations (50 μM, 100 μM, 500 μM, 1 mM, 5 mM, and 10 mM) of H_2O_2. The antibacterial activity of the nanomaterials was also tested by a colony

counting method. The above diluted bacterial suspension was mixed with different samples: PBS, H_2O_2, CuSA-loaded ZnS@MoS_2, CuSA-loaded ZnS@MoS_2 + H_2O_2, without and with 808 nm NIR laser irradiation for 10 min in the 2 mL of centrifuge tubes. The final concentrations of H_2O_2 and catalysts were 100 μM and 12.5 μg/mL, respectively. The other processes were the same as above.

Root plant pathogen (*R. solanacearum*): The antibacterial experiments were conducted following the previous methods[25]. Briefly, *R. solanacearum* cells were incubated in B medium (tryptone 10 g/L, yeast extract 1 g/L, and casein acid hydrolysate 1 g/L) with shaking at 28°C overnight. The obtained bacterial suspension (OD_{600} = 1.0) was diluted to 10^4. Then the bacterial suspension with different treatments (final concentrations: 0, 2.5, 5, 10, and 20 μg/mL) was directly inoculated onto the casamino acid peptone glucose (CPG) agar medium plates. The CFU on the agar plates was counted after cultivating for 48 h in an incubator. The inhibition rate (%) was calculated according to formula (2). Furthermore, the inhibition rates of different concentrations CuSA-loaded ZnS@MoS_2 nanozyme and thiodiazole copper against *R. solanacearum* were utilized to calculate the EC_{50} values.

The H_2O_2 concentration was optimized to investigate the antibacterial activity of CuSA-loaded ZnS@MoS_2 nanozyme based on its POD-like properties. The above diluted bacterial suspension was incubated with different concentrations (5, 10, 20, 30, 40, and 50 μM) of H_2O_2. The antibacterial activity of the nanomaterials was also tested by a colony-counting method. The above diluted bacterial suspension was mixed with different samples: PBS, H_2O_2, CuSA-loaded ZnS@MoS_2, and CuSA-loaded ZnS@MoS_2 + H_2O_2. The final concentrations of H_2O_2 and catalysts were 10 μM and 2.5 μg/mL, respectively. The other processes were the same as above.

Reporting summary

Further Information on research design is available in the Nature Portfolio Reporting Summary linked to this article.

Data availability

All raw sequence data reported in this paper have been deposited in the NCBI Sequence Reading Archive (SRA), with the BioProject login number PRJNA1372983 (http://www.ncbi.nlm.nih.gov/bioproject/1372983). DFT computational model data is provided in Supplementary Data 1. Source data are available for Figs. 1e-j, 2a-g, 3c, 4a-c, 4h-i, 5c-d and Supplementary Figs. 1, 3, 4, 7-12, 14-16, 21b, 22b, 23b, 24b, 25b, 26b, 27b, 28b, 30b, 31b, 32b, 33-39, 40c-d, 40g-h, 41a-d, 41g, 42-43, 44b-d, 45b-d, 46b-d, 47, 48b-c, 52-63, 64b, 66, 67b, 68, 69c, 70b, and 70d in the associated source data file. Source data are provided with this paper. All data underlying this study are available from the corresponding author upon request.

References

1. Yang, J. et al. Photo-stimuli smart supramolecular self-assembly of azobenzene/*β*-cyclodextrin inclusion complex for controlling plant bacterial diseases. *Adv. Funct. Mater.* **33**, 2303206 (2023).
2. Savary, S. et al. The global burden of pathogens and pests on major food crops. *Nat. Ecol. Evol.* **3**, 430-439 (2019).
3. Gu, S. et al. Competition for iron drives phytopathogen control by natural rhizosphere microbiomes. *Nat. Microbiol.* **5**, 1002-1010 (2020).
4. Griffin, K. et al. Copper-tolerance in *Pseudomonas syringae* pv. *tomato* and *Xanthomonas* spp. and the control of diseases associated with these pathogens in tomato and pepper. A systematic literature review. *Crop Prot.* **96**, 144-150 (2017).
5. Li, S. et al. Soil acidification aggravates the occurrence of bacterial wilt in South China. *Front. Microbiol.* **8**, 703 (2017).
6. Xu, H. et al. Design, synthesis and antifungal activities of novel *cis*-enamides via intermediate derivatization method. *Adv. Agrochem* **2**, 97-103 (2023).
7. Wang, D. et al. Nano-enabled pesticides for sustainable agriculture and global food security. *Nat. Nanotechnol.* **17**, 347-360 (2022).
8. Ai, Y. et al. Recent advances in nanozymes: From matters to bioapplications. *Adv. Funct. Mater.* **32**, 2110432 (2022).
9. Jiang, D. et al. Nanozyme: New horizons for responsive biomedical applications. *Chem. Soc. Rev.* **48**,

3683-3704 (2019).

10. Liu, Q. et al. A review on metal-and metal oxide-based nanozymes: Properties, mechanisms, and applications. *Nano-Micro Lett.* **13**, 1-53 (2021).
11. Ling, C. et al. Atomic-layered Cu_5 nanoclusters on FeS_2 with dual catalytic sites for efficient and selective H_2O_2 activation. *Angew. Chem. Int. Ed.* **134**, e202200670 (2022).
12. Yu, H. et al. Bi_2O_3/TiO_2@reduced graphene oxide with enzyme-like properties efficiently inactivates *Pseudomonas syringae* pv. tomato DC3000 and enhances abiotic stress tolerance in tomato. *Environ. Sci.: Nano* **9**, 118-132 (2022).
13. Yuan, Y. et al. Stable peptide-assembled nanozyme mimicking dual antifungal actions. *Nat. Commun.* **15**, 5636 (2024).
14. Huang, H. et al. Spiky artificial peroxidases with V-O-Fe pair sites for combating antibiotic-resistant pathogens. *Angew. Chem. Int. Ed.* **136**, e202310811 (2024).
15. van Bruggen, A. H. et al. Plant disease management in organic farming systems. *Pest Manag. Sci.* **72**, 30-44 (2016).
16. Camejo, D. et al. Reactive oxygen species, essential molecules, during plant-pathogen interactions. *Plant Physiol. Biochem.* **103**, 10-23 (2016).
17. Wu, H. et al. A photomodulable bacteriophage-spike nanozyme enables dually enhanced biofilm penetration and bacterial capture for photothermal-boosted catalytic therapy of MRSA infections. *Adv. Sci.* **10**, 2301694 (2023).
18. Fang, Y. et al. Near-infrared-responsive CuS@Cu-MOF nanocomposite with high foliar retention and extended persistence for controlling strawberry anthracnose. *J. Control. Release* **367**, 837-847 (2024).
19. Jiang, P. et al. Tuning oxidant and antioxidant activities of ceria by anchoring copper single-site for antibacterial application. *Nat. Commun.* **15**, 1010 (2024).
20. Chen, Y. et al. Thermal atomization of platinum nanoparticles into single atoms: An effective strategy for engineering high-performance nanozymes. *J. Am. Chem. Soc.* **143**, 18643-18651 (2021).
21. Wu, J. et al. Enhancing radiation-resistance and peroxidase-like activity of single-atom copper nanozyme via local coordination manipulation. *Nat. Commun.* **15**, 6174 (2024).
22. Geng, H. et al. Highly adhesive and catalytic VO_xC nanosheets with strong antibacterial activity. *Nano Today* **52**, 101989 (2023).
23. Ahmed, R. et al. Multivalent bacteria binding by flexible polycationic microsheets matching their surface charge density. *Adv. Mater. Interfaces* **7**, 1902066 (2020).
24. Xu, S. et al. Vacancies on 2D transition metal dichalcogenides elicit ferroptotic cell death. *Nat.*

Commun. **11**, 3484 (2020).

25. Liang, W. et al. pH-responsive on-demand alkaloids release from core-shell ZnO@ZIF-8 nanosphere for synergistic control of bacterial wilt disease. *ACS Nano* **16**, 2762-2773 (2022).
26. Ji, L. et al. One-pot synthesis of porous 1T-phase MoS_2 integrated with single-atom Cu doping for enhancing electrocatalytic hydrogen evolution reaction. *Appl. Catal. B: Environ.* **251**, 87-93 (2019).
27. Sawada, H. et al. Atomic-resolution STEM imaging of graphene at low voltage of 30 kV with resolution enhancement by using large convergence angle. *Phys. Rev. Lett.* **114**, 166102 (2015).
28. de Graaf, S. et al. Resolving hydrogen atoms at metal-metal hydride interfaces. *Sci. Adv.* **6**, eaay4312 (2020).
29. Liu, C. et al. Direct observation of oxygen atoms taking tetrahedral interstitial sites in medium-entropy body-centered-cubic solutions. *Adv. Mater.* **35**, 2209941 (2023).
30. Azam, A. et al. Formation and characterization of ZnO nanopowder synthesized by sol-gel method. *J. Alloy. Compd.* **496**, 399-402 (2010).
31. Wang, H. et al. Electrocatalytic determination of nitrite based on straw cellulose/molybdenum sulfide nanocomposite. *Biosens. Bioelectron.* **85**, 692-697 (2016).
32. Feng, C. et al. Effect of temperature on simultaneous separation and extraction of hemicellulose using *p*-toluenesulfonic acid treatment at atmospheric pressure. *Bioresour. Technol.* **348**, 126793 (2022).
33. Li, C. et al. SERS-and absorbance-based catalytic assay for determination of isocarbophos using aptamer-modified FeMOF nanozyme and in situ generated silver nanoparticles. *Microchim. Acta* **190**, 4 (2023).
34. Zhao, P. et al. A SERS nano-tag-based magnetic-separation strategy for highly sensitive immunoassay in unprocessed whole blood. *Talanta* **198**, 527-533 (2019).
35. Jacob, M. & Arof, A. FTIR studies of DMF plasticized polyvinyledene fluoride based polymer electrolytes. *Electrochim. Acta* **45**, 1701-1706 (2000).
36. Manthey, J. A. Fourier transform infrared spectroscopic analysis of the polymethoxylated flavone content of orange oil residues. *J. Agric. Food Chem.* **54**, 3215-3218 (2006).
37. Nie, W. et al. High sensitivity surface plasmon resonance biosensor for detection of microRNA based on gold nanoparticles-decorated molybdenum sulfide. *Anal. Chim. Acta* **993**, 55-62 (2017).
38. Song, Y. et al. Hydrothermal post-synthesis of HZSM-5 zeolite to enhance the coke-resistance of Mo/HZSM-5 catalyst for methane dehydroaromatization reaction: Reconstruction of pore structure and modification of acidity. *Appl. Catal. A-Gen.* **317**, 266-274 (2007).
39. McCreary, K. M. et al. Large-area synthesis of continuous and uniform MoS_2 monolayer films on

graphene. *Adv. Funct. Mater.* **24**, 6449-6454 (2014).

40. Ling, P. et al. Versatile three-dimensional porous Cu@Cu_2O aerogel networks as electrocatalysts and mimicking peroxidases. *Angew. Chem. Int. Ed.* **130**, 6935-6940 (2018).
41. Mamba, G. et al. Evidence for the degradation of an emerging pollutant by a mechanism involving iso-energetic charge transfer under visible light. *Appl Catal B-Environ*. **233**, 175-183 (2018).
42. Zhang, H. et al. *In situ* encapsulation engineering boosts the electrochemical performance of highly graphitized N-doped porous carbon-based copper-cobalt selenides for bifunctional oxygen electrocatalysis. *Nanoscale* **13**, 17663-17674 (2021).
43. Kozhevnikova, N. S. et al. One-pot green synthesis of copper sulfide (I) thin films with *p*-type conductivity. *Mater. Chem. Phys.* **242**, 122447 (2020).
44. Wang, J. H. et al. Three-dimensional zinc-seeded carbon nanofiber architectures as lightweight and flexible hosts for a highly reversible zinc metal anode. *ACS Nano* **17**, 19087-19097 (2023).
45. Li, H. et al. An efficient and stable inverted structure organic solar cell using ZnO modified by 2D $ZrSe_2$ as a composite electron transport layer. *Adv. Funct. Mater.* **34**, 2402128 (2024).
46. Suguna, A. et al. Design and fabrication of Zeolite Socony Mobil-5 incorporated ZnO composite for enhanced visible light photocatalytic performance. *Chem. Phys. Impact* **8**, 100621 (2024).
47. Yuan, H. et al. ZnO nanosheets abundant in oxygen vacancies derived from metal-organic frameworks for ppb-level gas sensing. *Adv. Mater.* **31**, 1807161 (2019).
48. Kloprogge, J. T. et al. XPS study of the major minerals in bauxite: Gibbsite, bayerite and (pseudo-)boehmite. *J. Colloid Interface Sci.* **296**, 572-576 (2006).
49. Lyu, L. et al. Selective H_2O_2 conversion to hydroxyl radicals in the electron-rich area of hydroxylated C-g-C_3N_4/CuCo-Al_2O_3. *J. Mater. Chem. A* **5**, 7153-7164 (2017).
50. Zhou, J. et al. Photothermally triggered copper payload release for cuproptosis-promoted cancer synergistic therapy. *Angew. Chem. Int. Ed.* **62**, e202213922 (2023).
51. Suganami, M. et al. Co-overproducing Rubisco and Rubisco activase enhances photosynthesis in the optimal temperature range in rice. *Plant Physiol.* **185**, 108-119 (2021).
52. Amiour, S. D. & Hambaba, L. Effect of pH, temperature and some chemicals on polyphenoloxidase and peroxidase activities in harvested Deglet Nour and Ghars dates. *Postharvest Biol. Technol.* **111**, 77-82 (2016).
53. Gu, Y. et al. Oxidase mimic graphdiyne for efficient superoxide generation in wide pH ranges. *Adv. Funct. Mater.* **32**, 2110192 (2022).
54. Wang, L. et al. Defect-rich adhesive molybdenum disulfide/rGO vertical heterostructures with

enhanced nanozyme activity for smart bacterial killing application. *Adv. Mater.* **32**, 2005423 (2020).
55. Yuan, H. et al. Exploration of the existence forms and patterns of dissolved oxygen molecules in water. *Nano-Micro Lett.* **16**, 1-13 (2024).
56. Dong, H. et al. Depletable peroxidase-like activity of Fe_3O_4 nanozymes accompanied with separate migration of electrons and iron ions. *Nat. Commun.* **13**, 5365 (2022).
57. Xu, D. et al. Rational design of MoS_2-supported Cu single-atom catalysts by machine learning potential for enhanced peroxidase-like activity. *Nanoscale* **15**, 6686-6695 (2023).
58. Nederberg, F. et al. Biodegradable nanostructures with selective lysis of microbial membranes. *Nat. Chem.* **3**, 409-414 (2011).
59. Zhao, L. et al. Nanobiotechnology-based strategies for enhanced crop stress resilience. *Nat. Food* **3**, 829-836 (2022).
60. Kah, M. et al. Nano-enabled strategies to enhance crop nutrition and protection. *Nat. Nanotechnol.* **14**, 532-540 (2019).
61. Pulizzi, F. Nano in the future of crops. *Nat. Nanotechnol.* **14**, 507-507 (2019).
62. Kurapati, R. et al. Enzymatic biodegradability of pristine and functionalized transition metal dichalcogenide MoS_2 nanosheets. *Adv. Funct. Mater.* **27**, 1605176 (2017).
63. Yuan, J. et al. Root exudates drive the soil-borne legacy of aboveground pathogen infection. *Microbiome* **6**, 1-12 (2018).
64. Li, J. et al. Molybdenum disulfide-supported cuprous oxide nanocomposite for near-infrared-I light-responsive synergistic antibacterial therapy. *ACS Nano* **18**, 16184-16198 (2024).
65. Gao, C. et al. A user-friendly herbicide derived from photo-responsive supramolecular vesicles. *Nat. Commun.* **9**, 2967 (2018).

Acknowledgements

This work was supported by the Scientific Research Project of Higher Education Department of Guizhou Province (Youth Project) (2022-116, L.C.) and the Guizhou University Natural Science Special Post Special Fund (2021-42, L.C.).

Author contributions statement

H.J. and L.C. conceived and designed the study and supervised the project. H.J. conducted experiments, analyzed the data, and wrote the initial manuscript. Y.X. and Z.F.M. performed nanomaterial

synthesis experiments and antibacterial experiments. L.C., G.J.F., Z.W.L., and S.Y. gave some suggestions for the study and advanced project direction. Z.W.L. provided technical support for both transmission electron microscopy and scanning electron microscopy. All the authors discussed the results and commented on the manuscript.

Competing interests statement

The authors declare no competing interests.

Figure captions

Fig. 1 Schematic illustration and structural characterization of CuSA-loaded ZnS@MoS_2 nanozyme. a Schematic of CuSA-loaded ZnS@MoS_2 nanozyme synthesis. (Blue: Cu single atom) **b-d** TEM, HAADF-STEM, and HAADF-STEM elemental mapping representative images of CuSA-loaded ZnS@MoS_2 nanozyme (each experiment was repeated three times independently with similar results). **e** K-edge XANES spectra of Cu. **f** FT of Cu K-edge EXAFS of samples in R space. **g** The corresponding EXAFS fitting curves of CuSA-loaded ZnS@MoS_2 at K space. **h-j** WT-EXAFS plots of CuO, CuS, and CuSA-loaded ZnS@MoS_2. Source data are provided as a Source Data file.

Fig. 2 Photothermal enhanced POD-like activity of CuSA-loaded ZnS@MoS_2 nanozyme. a The temperature rise of CuSA-loaded ZnS@MoS_2 solution under 1.00 W/cm^2 808 nm laser irradiation at different concentrations within 10 min. Data are presented as mean ± SD (n = 3 independent experiments). **b** Calculated photothermal conversion efficiency of CuSA-loaded ZnS@MoS_2 upon 1.00 W/cm^2 NIR-808 nm laser irradiation. Data are presented as mean ± SD (n = 3 independent experiments). **c** UV-vis absorption spectra of TMB solution containing different samples with or without 1.00 W/cm^2 NIR-808 nm laser irradiation. **d-e** Steady-state kinetic assay of POD-like activity of CuSA-loaded ZnS@MoS_2 nanozyme with varied TMB and H_2O_2. Data are presented as mean ± SD (n = 3 independent experiments). **f** Comparison of the TON and V_{max} values with previous POD-like nanozymes. **g** EPR spectra of ·OH

trapped DMPO with different treatments. **h** Schematic illustration of laser-enhanced POD-like activity of CuSA-loaded ZnS@MoS_2 nanozyme. Source data are provided as a Source Data file.

Fig. 3 Catalytic mechanism of CuSA-loaded ZnS@MoS_2. a The structure of CuSA-loaded ZnS@MoS_2 with Cu-N/O coordination. **b** The structure of CuSA-loaded ZnS@MoS_2 with Cu-S coordination. **c** The energy distribution for the generation of ·OH from H_2O_2 catalyzed by CuSA-loaded ZnS@MoS_2 in two distinct coordination environments. **d-e** The structural changes of CuSA-loaded ZnS@MoS_2 with two distinct coordination environments during the reaction pathway. **f** Behavior of electrons of CuSA-loaded ZnS@MoS_2 catalyzing H_2O_2 to release ·OH. Source data are provided as a Source Data file.

Fig. 4 *In vitro* antibacterial activity and mechanism of CuSA-loaded ZnS@MoS_2 nanozyme. a Inhibition rate of *Pst*. DC3000 after different concentrations of thiodiazole copper and CuSA-loaded ZnS@MoS_2 nanozyme. Data are presented as mean ± SD (n = 3 biological replicates). The asterisk denotes a significant difference as determined by the independent *t*-test (two-sided, *$p < 0.05$, **$p < 0.01$, and ***$p < 0.001$). 12.5 μg/mL ($t = 6.093$, df = 4, $p = 0.004$), 25 μg/mL ($t = 30.107$, df = 4, $p < 0.001$), 50 μg/mL ($t = 30.707$, df = 4, $p < 0.001$), 100 μg/mL ($t = 53.942$, df = 4, $p < 0.001$), and 200 μg/mL ($t = 17.631$, df = 2.001, $p = 0.003$). **b** Inhibition rate of *Pst*. DC3000 after different treatments. The wavelength of the NIR irradiation was set at 808 nm, with an intensity of 1.00 W/cm^2, and an irradiation time of 10 min. Data are presented as mean ± SD (n = 3 biological replicates). All values marked with different letters are significantly different among different treatment groups at $p < 0.05$ as determined by one-way ANOVA with Tukey HSD test (Inhibition rate: $F_{6, 14} = 3698.097$, $p < 0.001$). All values marked with same letters indicate no significant difference among different treatment groups. **c** Bacteria inhibition rate of *R. solanacearum* after different concentrations of thiodiazole copper and CuSA-loaded ZnS@MoS_2 nanozyme. Data are presented as mean ± SD (n = 3 biological replicates). The asterisk denotes a significant difference as determined by the independent *t*-test (two-sided, *$p < 0.05$, **$p < 0.01$, and ***$p < 0.001$). 2.5 μg/mL ($t = 22.861$, df = 4, $p < 0.001$), 5 μg/mL ($t = 115.865$, df = 4, $p < 0.001$), 10 μg/mL

(t = 55.2, df = 4, p < 0.001), and 20 μg/mL (t = 101.485, df = 2, p < 0.001). **d-e** ROS staining fluorescence representative images of *Pst*. DC3000 and *R. solanacearum* after different treatments (each experiment was repeated three times independently with similar results). Scar bar: 20 μm. The wavelength of the NIR irradiation was set at 808 nm, with an intensity of 1.00 W/cm^2, and an irradiation time of 10 min. **f-g** SEM representative images of *Pst*. DC3000 and *R. solanacearum* after different treatments (each experiment was repeated three times independently with similar results). The wavelength of the NIR irradiation was set at 808 nm, with an intensity of 1.00 W/cm^2, and an irradiation time of 10 min. **h-i** Interaction mechanism of CuSA-loaded ZnS@MoS_2 nanozyme with the Gram-negative bacterial cell membrane surface was calculated by DFT. **j** Schematic illustration of antibacterial mechanisms. Source data are provided as a Source Data file.

Fig. 5 *In vivo* antibacterial properties of CuSA-loaded ZnS@MoS_2 nanozyme. a Representative photographs 7 dpi after different foliar application (sterile water, 55 μg/mL ZnO NPs, 23.8 μg/mL MoS_2 nanosheets, 22.8 μg/mL CuO NPs, 200 μg/mL thiodiazole copper, and 200 μg/mL CuSA-loaded ZnS@MoS_2 nanozyme). **b** Representative photographs 10 dpi after different root application (sterile water, 5.5 μg/mL ZnO NPs, 2.38 μg/mL MoS_2 nanosheets, 2.28 μg/mL CuO NPs, 20 μg/mL thiodiazole copper, and 20 μg/mL CuSA-loaded ZnS@MoS_2 nanozyme). **c-d** Disease index of tomato speck disease and tomato wilt disease after different treatments. Data are presented as mean ± SD (n = 3 biological replicates). All values marked with different letters are significantly different among different treatment groups at p < 0.05. Disease index of tomato speck disease: $F_{5, 12}$ = 68.3, p < 0.001; disease index of tomato wilt disease: $F_{5, 12}$ = 33.318, p < 0.001. All values marked with same letters indicate no significant difference among different treatment groups. Source data are provided as a Source Data file.

Nanozymes are promising for controlling plant bacterial diseases, but conventional nanozymes suffer from low

bacterial affinity, inefficient enzyme-like activity, and thus poor antibacterial efficacy. Here, the authors report a copper single-atom nanozyme that outperforms commercial thiodiazole copper in controlling plant bacterial diseases via intelligent capture and photo-enhanced activity.

Peer Review Information: *Nature Communications* thanks Sumati Bhatia, and the other, anonymous, reviewer(s) for their contribution to the peer review of this work. A peer review file is available.

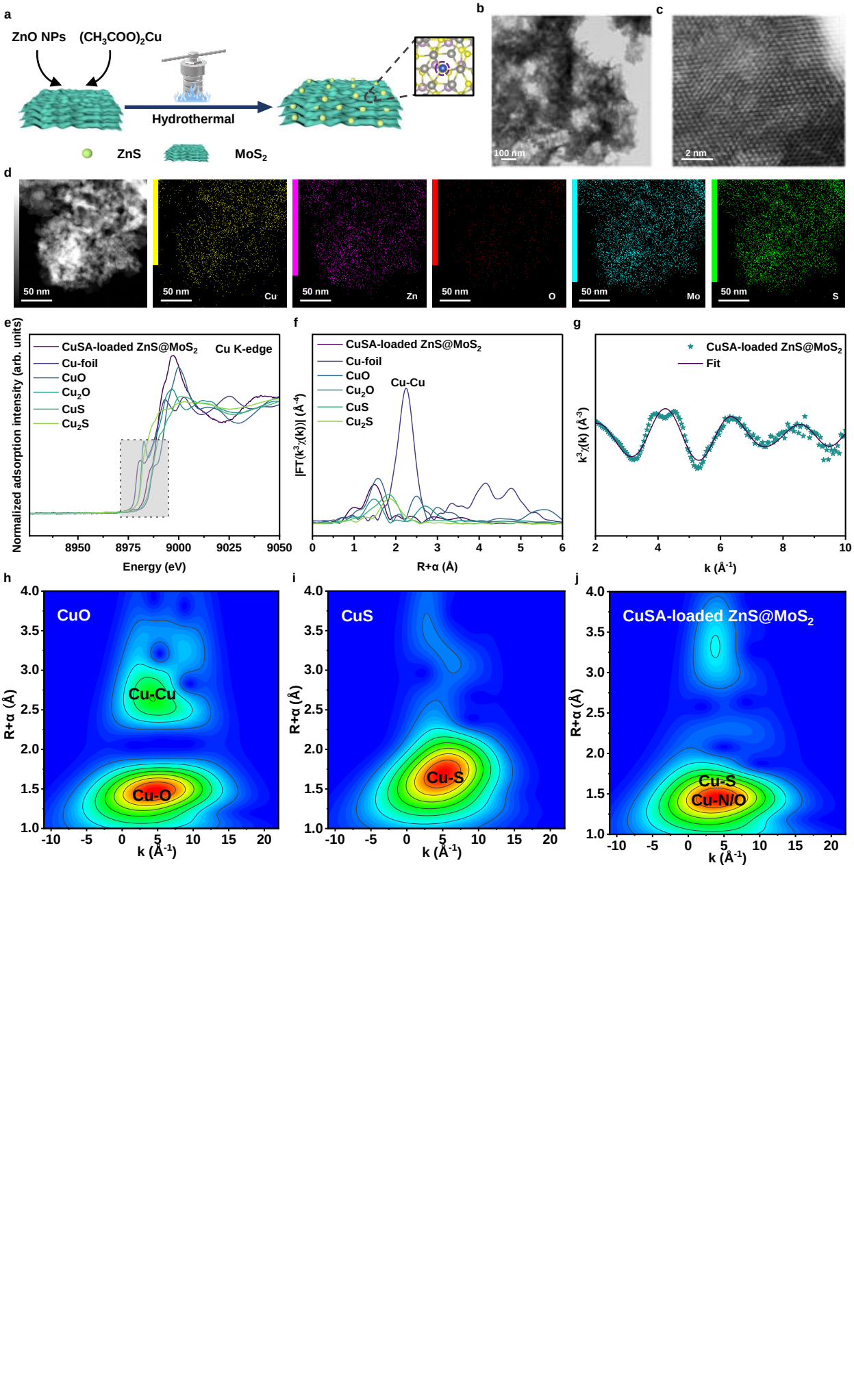
a
ZnO NPs
(CH3COO)2Cu
Hydrothermal
ZnS
MoS2
b
100 nm
c
2 nm
d
50 nm
Cu
Zn
O
Mo
S
e
CuSA-loaded ZnS@MoS2
Cu K-edge
Cu-foil
CuO
Cu2O
CuS
Cu2S
Normalized adsorption intensity (arb. units)
Energy (eV)
f
Cu-Cu
|FT(k3χ(k))| (Å-4)
R+α (Å)
g
Fit
k3χ(k) (Å-3)
k (Å-1)
h
CuO
Cu-Cu
Cu-O
R+α (Å)
k (Å-1)
i
CuS
Cu-S
j
Cu-S
Cu-N/O

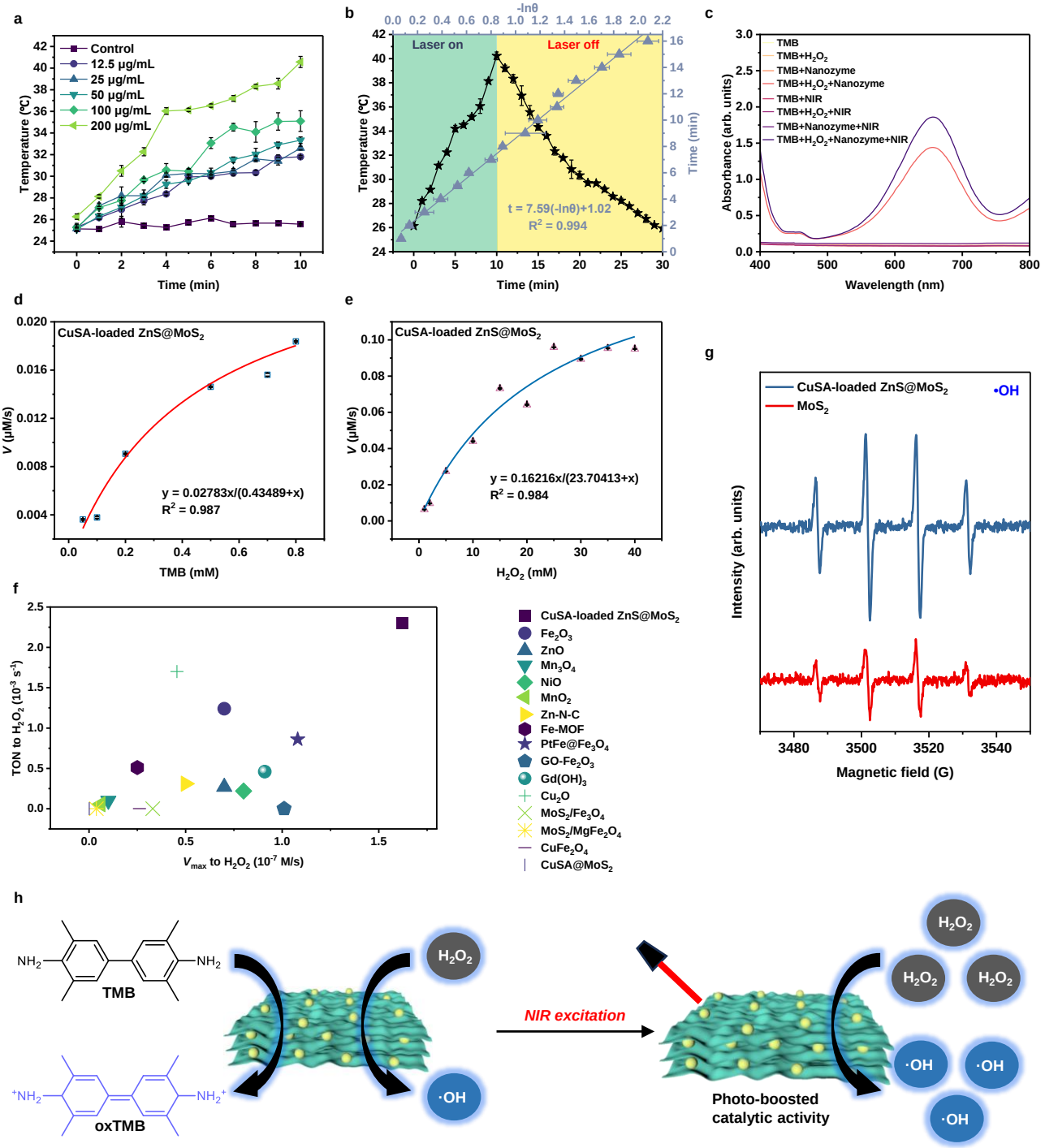
a
Control
12.5 μg/mL
25 μg/mL
50 μg/mL
100 μg/mL
200 μg/mL
Temperature (℃)
Time (min)
b
-lnθ
Laser on
Laser off
t = 7.59(-lnθ)+1.02
R² = 0.994
Temperature (℃)
Time (min)
c
TMB
TMB+H2O2
TMB+Nanozyme
TMB+H2O2+Nanozyme
TMB+NIR
TMB+H2O2+NIR
TMB+Nanozyme+NIR
TMB+H2O2+Nanozyme+NIR
Absorbance (arb. units)
Wavelength (nm)
d
CuSA-loaded ZnS@MoS2
y = 0.02783x/(0.43489+x)
R² = 0.987
V (μM/s)
TMB (mM)
e
CuSA-loaded ZnS@MoS2
y = 0.16216x/(23.70413+x)
R² = 0.984
V (μM/s)
H2O2 (mM)
g
CuSA-loaded ZnS@MoS2
MoS2
•OH
Intensity (arb. units)
Magnetic field (G)
f
TON to H2O2 (10-3 s-1)
Vmax to H2O2 (10-7 M/s)
CuSA-loaded ZnS@MoS2
Fe2O3
ZnO
Mn3O4
NiO
MnO2
Zn-N-C
Fe-MOF
PtFe@Fe3O4
GO-Fe2O3
Gd(OH)3
Cu2O
MoS2/Fe3O4
MoS2/MgFe2O4
CuFe2O4
CuSA@MoS2
h
TMB
oxTMB
H2O2
·OH
NIR excitation
Photo-boosted
catalytic activity

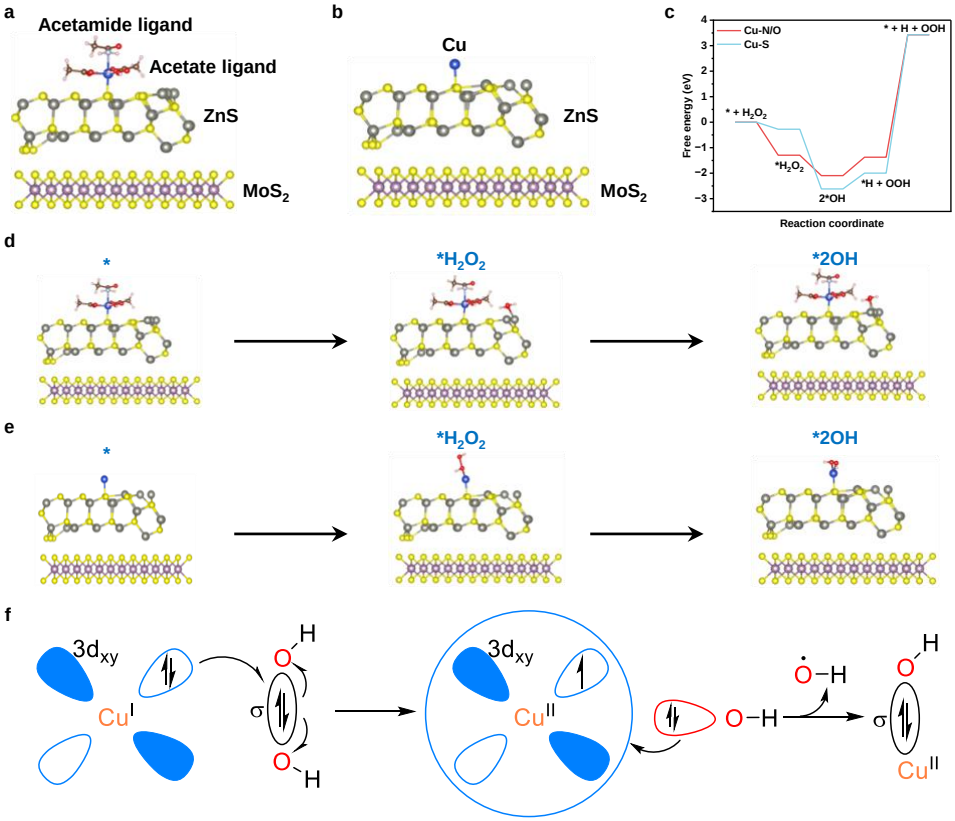
a
Acetamide ligand
Acetate ligand
ZnS
MoS2
b
Cu
ZnS
MoS2
c
Cu-N/O
Cu-S
* + H + OOH
Free energy (eV)
* + H2O2
*H2O2
2*OH
*H + OOH
Reaction coordinate
d
*
*H2O2
*2OH
e
*
*H2O2
*2OH
f
3dxy
CuI
σ
H
O
O
H
3dxy
CuII
O−H
O−H
O
H
σ
CuII

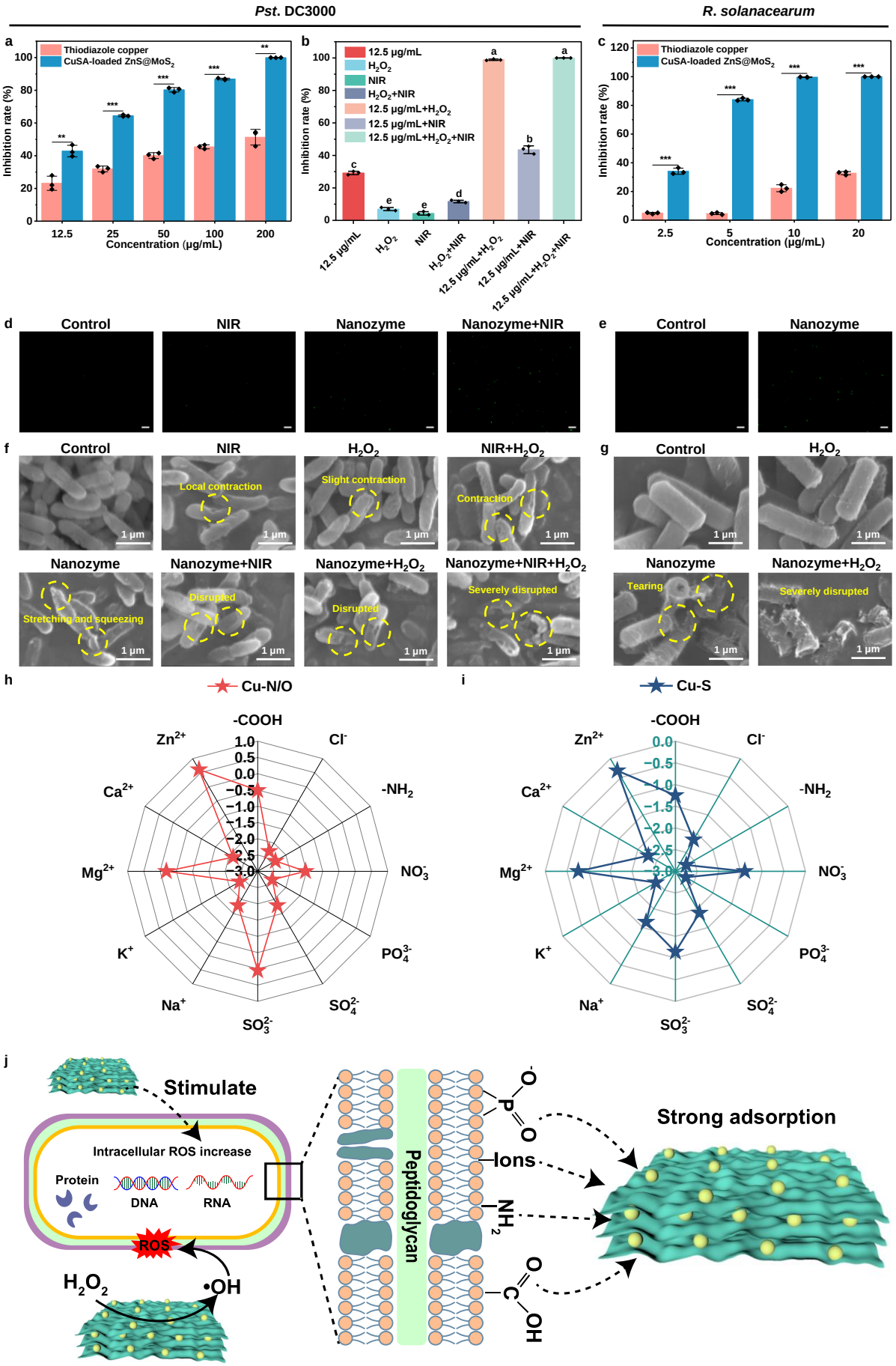
Pst. DC3000
R. solanacearum
a
Thiodiazole copper
CuSA-loaded ZnS@MoS2
Inhibition rate (%)
Concentration (μg/mL)
b
12.5 μg/mL
H2O2
NIR
H2O2+NIR
12.5 μg/mL+H2O2
12.5 μg/mL+NIR
12.5 μg/mL+H2O2+NIR
c
d
Control
NIR
Nanozyme
Nanozyme+NIR
e
f
H2O2
NIR+H2O2
Local contraction
Slight contraction
Contraction
Stretching and squeezing
Disrupted
Severely disrupted
g
Tearing
Nanozyme+H2O2
Nanozyme+NIR+H2O2
h
Cu-N/O
i
Cu-S
-COOH
Cl-
-NH2
NO3-
PO43-
SO42-
SO32-
Na+
K+
Mg2+
Ca2+
Zn2+
j
Stimulate
Intracellular ROS increase
Protein
DNA
RNA
ROS
H2O2
•OH
Peptidoglycan
Ions
Strong adsorption

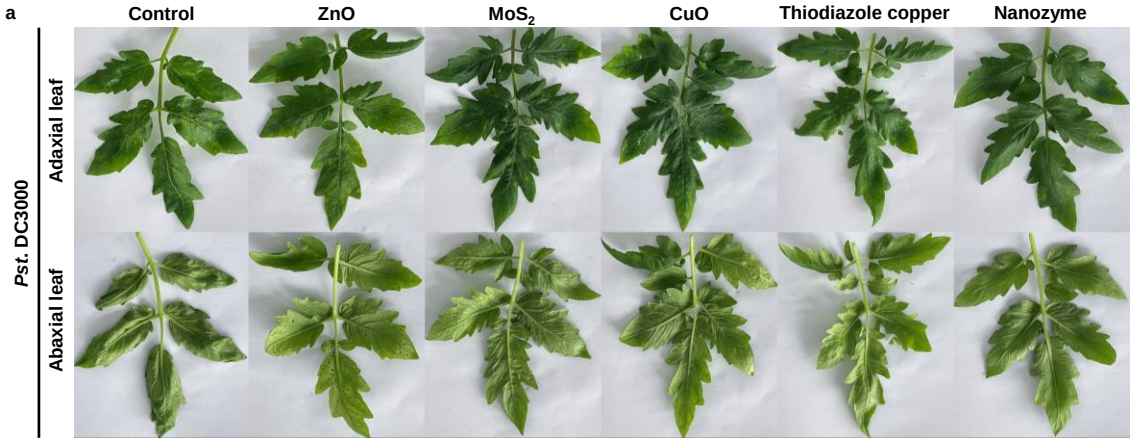
a
Control
ZnO
MoS2
CuO
Thiodiazole copper
Nanozyme
Pst. DC3000
Adaxial leaf
Abaxial leaf

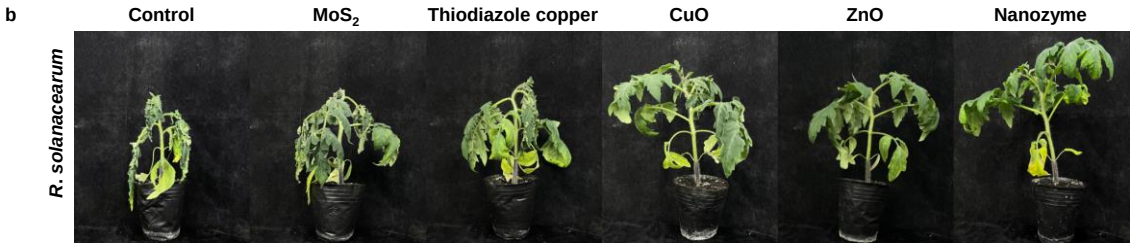
b
Control
MoS2
Thiodiazole copper
CuO
ZnO
Nanozyme
R. solanacearum

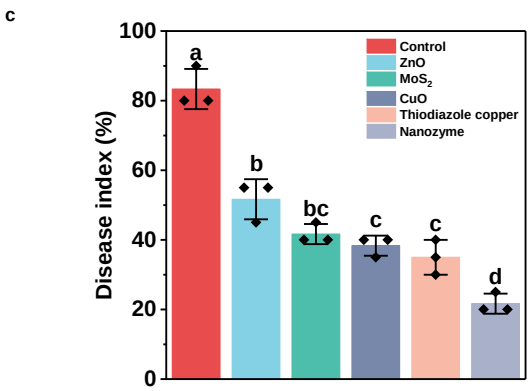
c
Disease index (%)
100
80
60
40
20
0
a
b
bc
c
c
d
Control
ZnO
MoS2
CuO
Thiodiazole copper
Nanozyme

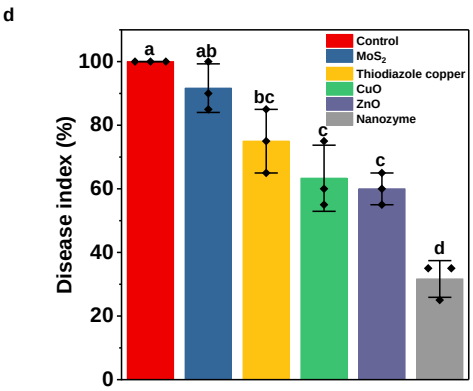
d
Disease index (%)
100
80
60
40
20
0
a
ab
bc
c
c
d
Control
MoS2
Thiodiazole copper
CuO
ZnO
Nanozyme